Design and Performance Assessment of an Integrated Flywheel Energy Storage Systems based on an Inner-Rotor Large-Airgap SPM

Andrea Floris, Alfonso Damiano, Alessandro Serpi

Abstract –**An integrated flywheel energy storage system topology is presented in this paper, which is based on an inner-rotor large-airgap surface-mounted permanent magnet synchronous machine and which aims at achieving a unity energy to power ratio. The proposed synchronous machine is equipped with a thick carbon-fiber cylindric layer that acts as both the flywheel and the sleeve; as a result, this layer ensures permanent magnet containment and storing/delivering the required amount of energy simultaneously. In order to comply with all the design targets and constraints, a two-step design procedure is employed: a preliminary design is achieved analytically, by using an integrated mechanical-electromagnetic-energy modelling. Subsequently, the preliminary configuration is refined and validated through finite element analyses, which regard a performance assessment on mechanical, electromagnetic, energy, and thermal aspects at different operating conditions.**

Index Terms —**Finite element analysis, Flywheels, Integrated design, Modeling, Permanent magnet machines**

I. INTRODUCTION

Energy Storage Systems (ESSs) play a key role in modern power systems, allowing for a number of grid services, among which load levelling, frequency regulation, peak shaving and transient stability [1], [2]. Different ESS technologies have been proposed in the literature depending on the specific application, among which the most popular are electrochemical batteries, supercapacitors and Flywheel ESSs (FESSs) [1], [3], [4]. In particular, FESS represents a viable alternative to both batteries and supercapacitors due to its high dynamic response, low maintenance, long lifecycle, high efficiency and low environmental impact. On the other hand, FESS suffers from self-discharge rates much higher than other ESSs, and its design and manufacturing require advanced knowledge on different electromagnetic and mechanical aspects.

Despite sharing almost the same elements, several FESS configurations have been proposed in the literature, which can be roughly classified in split and integrated topologies [5]. In the latter, the flywheel is integrated within the rotor of the electrical machine at the aim of minimizing volume, weight and costs, increasing the efficiency and reducing the overall losses as well. These advantages could be more evident if a Surface-Mounted Permanent Magnet Synchronous Machine (SPM) with an inner rotor structure is adopted [6], [7]. This configuration presents both advantages and drawbacks compared to its counterpart (outer-rotor SPM), particularly a large equivalent airgap is needed, especially if a relatively high energy content is required, causing a significant PM flux leakage and, thus, reduced torque density. This issue does not occur in outer-rotor SPM, which, however, maybe characterized by relatively large inner and outer rotor diameters, which could prevent the achievement of high rotating speeds. Moreover, the outer stator in inner-rotor SPM acts as a preliminary enclosure, thus increasing safety of the overall FESS.

In this context, the design of an integrated FESS topology consisting of an Inner-Rotor Large-Airgap Surface-Mounted Permanent Magnet Synchronous Machine (IRLA-SPM) is presented in this paper. In particular, the proposed FESS needs to store a relatively high amount of energy compared to its rated power (8 kWh vs 8 kW). This results into an inner-rotor SPM characterized by a large equivalent airgap, most of which is represented by the thick carbon-fiber cylindrical layer required for matching the energy constraint above mentioned. The preliminary design of IRLA-SPM is carried out by means of a multi-parameter analytical design procedure [8]–[10], which guarantees the compliance with all design specifications and constraints through appropriate mechanical, electromagnetic, and energy modeling. Moreover, the design procedure enables minimizing the axial length, making the overall FESS suited for transportation and installation, by avoiding mechanical resonance phenomena at the same time. The proposed configuration is validated through extensive Finite Element Analyses (FEAs), which regard electromagnetic, mechanical, energy, and thermal performance assessments at different operating conditions.

II. FESS OVERVIEW

A. System description

A schematic representation of the proposed FESS configuration is depicted in Fig. 1, together with its main geometric dimensions, while material parameters are reported in Table I. The overall system should store 8 kWh of usable energy at 8 kW rated power, which are both set as design targets in order to make the designed FESS similar to electrochemical batteries for residential prosumers in terms of power and energy capability. Additionally, the system should be as flat as possible in order to be transported and installed relatively easily. For this reason, minimum FESS axial length is imposed as a design target.

The FESS rotor consists of several cylindric layers, among which the PM ring and the flywheel/sleeve; in this regard, the

This work has been developed within the project KINITIKI, which has been funded by the Sardinian Regional Government through Sardegna Ricerche under the Grant Agreement no. 1C-170 (Aids to R&D projects, POR FESR 2014-2020, Action 1.1.3).

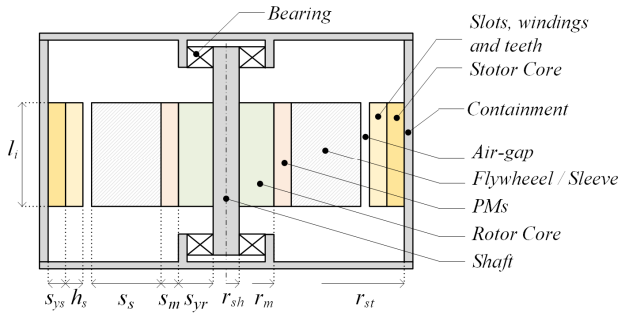

Fig. 1. Schematic representation of the integrated FESS topology considered in this paper.

TABLE I FESS MATERIAL PROPERTIES

Description	Symbol	Unit	Value
Flywheel/Sleeve (CFRP 60%)			
Specific mass density	$\rho^{(s)}$	kg/m^3	1500
Radial Young's modulus	$E^{(s)}_r$	MPa	150000
Tangential Young's modulus	$E^{(s)}_\theta$	MPa	10000
Radial Poisson's ratio	$\upsilon^{(s)}_r$	-	0.34
Tangential Poisson's ratio	$\upsilon^{(s)}_\theta$	-	0.02
Max radial tensile stress	$\sigma^{(s)}_{r,max\_t}$	MPa	10
Max radial compression stress	$\sigma^{(s)}_{r,max\_c}$	MPa	200
Max tangential tensile stress	$\sigma^{(s)}_{\theta,max\_t}$	MPa	2400
Max tangential compression stress	$\sigma^{(s)}_{\theta,max\_c}$	MPa	1200
Rotor and Stator Cores (M235-35A)			
Specific mass density	$\rho^{(yr)}$	kg/m^3	7600
Radial Young's modulus	$E^{(yr)}$	MPa	185000
Radial Poisson's ratio	$\upsilon^{(yr)}$	-	0.30
Max stress	$\sigma^{(yr)}_{max}$	MPa	700
Permanent Magnets (ferrite)			
Specific mass density	$\rho^{(m)}$	kg/m^3	5000
Radial Young's modulus	$E^{(m)}$	MPa	180000
Radial Poisson's ratio	$\upsilon^{(m)}$	-	0.28
Max tensile stress	$\sigma^{(m)}_{max\_t}$	MPa	60
Max compression stress	$\sigma^{(m)}_{max\_c}$	MPa	600
Magnetic remanence	$Br_{(m)}$	T	0.4

number of magnetic poles is set to 2 in order to enable high-speed operation by limiting electrical frequency and the related losses properly. Similarly, ferrite PMs are chosen not only to address PM cost and availability issues, but also due to their very low eddy-current losses compared to NdFeB solutions. The flywheel/sleeve is instead made up of carbon-epoxy composite with unidirectional circumferential fiber distribution, which maximizes the resistance and stiffness in circumferential direction, thus best fitting the typical stress distribution in rotating cylindrical components [11]. Furthermore, the flywheel/sleeve is prestressed in order to increase mechanical retention of PMs at high-speed operation.

Regarding the stator, a conventional three-phase winding is employed, while the silicon laminated steel M235-35A manufactured by Sura is chosen, especially for its very low specific losses at different frequencies of the magnetic flux density.

B. Design procedure

The design of IRLA-SPM has been achieved through a multi-parameter analytical design procedure [8]–[10], whose flowchart is depicted in Fig. 2. The procedure starts from a number of tunable variables, which are summarized in Table II; these can vary within appropriate ranges that are determined a priori based on the expected FESS size and performance. Tunable variables concur with design targets and material properties to determine derived variables through appropriate modelling. As a result, a number of IRLA-SPM configurations are achieved, each of which is represented by a multi-dimensional array of variables. All these configurations are then processed in order to verify their compliance with all operating constraints: these consist mainly of mechanical, electromagnetic, and energy relationships, as detailed in the following section. Among all the remaining IRLA-SPM configurations, the final geometry is selected by means of an optimization criterion, which is, in this case, the minimum axial length.

III. DESIGN CONSTRAINTS

A. Mechanical constraints

From a mechanical point of view, the flywheel/sleeve design represents a key issue for IRLA-SPM due to the large thickness of the carbon-fibre layer (s) needed for storing the required amount of energy. In this regard, the low mechanical resistance of the epoxy-matrix in radial direction limits the maximum thickness of this layer. Therefore, a multi-rim structure is adopted, which involves more cylindrical elements coupled to each other with interference [12], [13].

For the proper evaluation of the mechanical stress acting on the flywheel/sleeve, an advanced mechanical modelling of orthotropic materials is implemented. In addition, the stress acting on the other rotor layers is considered, namely the rotor yoke (yr) and the PM ring (m), because all of them has to comply with the following relationship:

$$\left|\sigma_x^{(y)}\right| < \left|s_f\,\sigma_{x,\max}^{(y)}\right|, \quad x \in \{r,\theta\}, \quad y \in \{yr,m,s\} \tag{1}$$

in which $\sigma_r^{(y)}$ and $\sigma_\theta^{(y)}$ represent the radial and tangential stress acting on the generic layer (y), $\sigma_{x,max}$ represents the maximum allowable stress of the material along the direction x, and s_f is a safety coefficient, generally assumed less than one in order to account for manufacturing tolerance and imperfections. The general expression of σ_r and σ_θ can be obtained by the analytical mechanical model based on the mechanic-elastic theory applied to a generic rotating pressurized cylinder [9], [14], resulting in the following relationships:

$$\sigma_r(r) = c_1 r^{k-1} + c_2 r^{-k-1} - \frac{(3+\upsilon_\theta)\rho\omega^2 r^2}{9-k^2} + \\ - E_\theta\left(\frac{r(2\alpha_\theta-\alpha_r)t}{4-k^2} + \frac{(\alpha_\theta-\alpha_r)t_0}{1-k^2}\right) \tag{2}$$

$$\sigma_\theta(r) = kc_1 r^{k-1} - kc_2 r^{-k-1} - \rho\omega^2 r^2\left(\frac{3(3+\upsilon_\theta)}{9-k^2} - 1\right) + \\ - E_\theta\left(\frac{2r(2\alpha_\theta-\alpha_r)t}{4-k^2} + \frac{(\alpha_\theta-\alpha_r)t_0}{1-k^2}\right) \tag{3}$$

where $E_{r/\theta}$ ($\upsilon_{r/\theta}$) is the Young's modulus (Poisson's ratio) along radial/tangential direction, $\alpha_{r/\theta}$ is the thermal expansion coefficients along radial/tangential direction, while c_1, c_2, t_0 and t are constant coefficients that depend on the inner and outer cylinder pressures, rotating speed and temperature gradient. Furthermore, k is defined as:

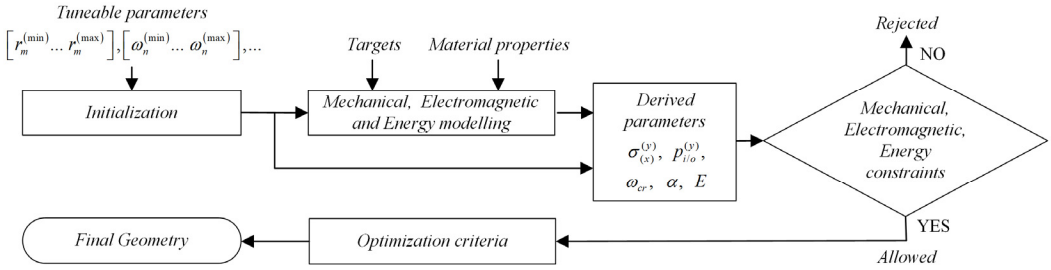

Fig. 2. Flowchart of the multi-parameter analytical design procedure used for designing IRLA-SPM.

TABLE II IRLA-SPM DESIGN VARIABLES

	Variable	Symbol	Unit
Tuneable	Inner PM radius	r_m	mm
	PM thickness	s_m	mm
	Sleeve thickness	s_s	mm
	Sleeve interference fit	δ	mm
	Active length	l_i	mm
	Rated speed	$\omega_{m,n}$	rpm
	Speed ratio ($\omega_{m,max}/\omega_{m,n}$)	$\Delta\omega_m$	-
Derived	Radial and tangential stress	$\sigma_{r/\theta}^{(y)}$	MPa
	Contact pressure	$p_{i/o}^{(y)}$	MPa
	Rotor critical speed	ω_{cr}	rpm
	Magnetic ratio	α	-
	Storable/deliverable energy	E	kWh

$$k = \sqrt{E_\theta / E_r} \ . \tag{4}$$

In order to guarantee appropriate adhesion between each pair of rotor layers at any operating condition, it is necessary to impose that internal/external contact pressures ($p_{i/o}$) acting on each rotor layer are always greater than zero:

$$p_{i/o}^{(y)} > 0, \quad y \in \{yr, m, s\} \ . \tag{5}$$

Referring to Fig. 3, the expression of contact pressures $p_i^{(y)}$ and $p_o^{(y)}$ can be obtained starting from the radial displacement u_r of each rotor layer, which is defined by the Hooke's law as

$$u_r^{(y)} = \frac{r}{E_\theta^{(y)}}\left(\sigma_\theta^{(y)} - k\upsilon_r^{(y)}\sigma_r^{(y)} + E_\theta^{(y)}\alpha_\theta^{(y)}\Delta T^{(y)}\right) \tag{6}$$

in which ΔT is the difference between actual and reference temperature in each rotor layer. Then, the radial deflection on the contact surfaces between different layers is

$$\begin{aligned} &\left(u_r^{(s_j)} - u_r^{(s_{j-1})}\right)\Big|_{r=r_{s_j}} = \delta_j \ , \qquad j \in \{2 \div n_{rim}\} \\ &\left(u_r^{(s_1)} - u_r^{(m)}\right)\Big|_{r=r_m} = \delta_1 \ , \qquad \left(u_r^{(m)} - u_r^{(yr)}\right)\Big|_{r=r_{yr}} = 0 \end{aligned} \tag{7}$$

in which δ_1 and δ_j are the radial interferences between the different layers, i.e. the difference between the outer radius of a layer and the free inner radius of the following adjoining layer, while n_{rim} is the number of rims. Therefore, based on (2)-(4) and (6)-(7), the pressure distribution among the rotor layers can be achieved by imposing the following boundary conditions:

$$\begin{cases} p_i^{(yr)} = 0 \\ p_o^{(yr)} = -p_i^{(m)} \end{cases}, \quad \begin{cases} p_o^{(m)} = -p_i^{(s_1)} \\ p_o^{(s_{j-1})} = -p_i^{(s_j)} \\ p_o^{(s_{n_{rim}})} = 0 \end{cases} . \tag{8}$$

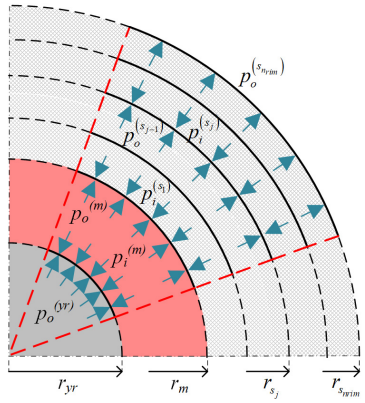

Fig. 3. Contact pressures acting on the different rotor layers.

Apart from stress and pressure constraints, mechanical resonance phenomena should be accounted as well, which requires that the critical speed ω_{cr} must be reasonably higher than the IRLA-SPM maximum speed, leading to

$$\omega_{m,\max} \ll \omega_{cr} \ , \quad \omega_{cr} = \sqrt{k_s / M} \tag{9}$$

in which k_s is stiffness of the shaft to transverse vibrations and M is the rotor mass.

B. *Electromagnetic constraints*

From an electromagnetic point of view, PM demagnetization has to be prevented at any operating condition, by enabling an adequate flux-weakening capability at the same time. Therefore, referring to the magnetic flux densities due to stator *mmf* ($\tilde{B}_m$) and PMs ($\bar{B}_m$) separately, the following relationship is imposed [9]:

$$\tilde{B}_m = \alpha \bar{B}_m \tag{10}$$

in which α denotes the magnetic ratio, which should be within (0,1). Regarding $\tilde{B}_m$ and $\bar{B}_m$, their general expressions can be achieved by applying both Ampere's and Gauss' laws under some assumptions [9], leading to:

$$\tilde{B}_m \propto n \cdot I_{eq} \ , \quad \bar{B}_m \propto -2 s_m H_c \tag{11}$$

where n and I_{eq} are the equivalent turns and current of the machine winding, whose product represents the overall stator *mmf*, while H_c is the PM coercive force. Consequently, by substituting (11) into (10), the following inequality is achieved:

$$-\frac{n \cdot I_{eq}}{2 s_m H_c} \le \alpha^* \tag{12}$$

where α^* is the maximum allowable value of α in order to prevent PM demagnetization safely [9].

C. Energy constraints

The energy requirement is guaranteed by the following relationship:

$$E_{rotor}\big|_{\omega_{m,max}} - E_{rotor}\big|_{\omega_{m,n}} \geq E^* \tag{13}$$

in which E_{rotor} denotes the energy stored by the IRLA-SPM rotor at a given speed, while E^* is the amount of energy that should be exchanged by FESS over its full operating range (8 kWh, from $\omega_{m,min}$ to $\omega_{m,max}$ and vice versa). Particularly, it is worth noting that the FESS minimum operating speed is set at the rated speed ($\omega_{m,n}$) in order to always operate within the constant-power region. Moreover, E_{rotor} can be expressed as

$$E_{rotor} = \frac{1}{2} J \omega_m^{\,2} \tag{14}$$

where J represents the inertia coefficient of the rotor mass. As a result, substituting (14) in (13) yields

$$\omega_{m,\max}^2 - \omega_{m,n}^2 \geq \frac{2E^*}{J}\,. \tag{15}$$

IV. Analytical Results and FEA Analyses

The main design parameters of the final geometry of the proposed IRLA-SPM and its rated values are summarized in Table III. In particular, $\omega_{m,min}$ has been set to $\omega_{m,n}$ in order to enable FESS to always deliver/absorb the required amount of energy (8 kWh) at rated power.

Regarding the flywheel/sleeve, this is made up of 7 rims with increasing interferences (from 0.2 mm to 0.9 mm), which are needed in order to satisfy mechanical and energy constraints simultaneously. This aspect is well highlighted in Fig. 4, which shows the distribution of σ_r and σ_θ in the rotor along the radial direction at the maximum speed (18 krpm); due to the multi-rim structure, the maximum stress is always within the limits of the materials, even by considering an adequate safety factor equal to 0.5. In addition, Fig. 4 shows some discontinuities in stress evolutions, which correspond to the contact surfaces between the different rims.

A first validation of the proposed IRLA-SPM has been then carried out by Finite-Element Analyses (FEAs), which regard mechanical, electromagnetic, energy, and thermal aspects, as detailed in the following.

A. Mechanical FEA

Mechanical FEA focuses on the mechanical forces acting on the overall rotor, i.e. $\sigma_{\theta,r}$ and $p_{i/o}$ distributions. Particularly, the distribution of σ_θ at $\omega_{m,max}$ is shown in Fig. 5. It can be seen that σ_θ is higher on the inner surface of the outer rim, and it decreases with radial displacement in the inner layers, as expected. The maximum value achieved for tangential stress is about 1100 MPa, which well matches that obtained analytically (Fig. 4). In addition, this value is much lower than the maximum stress allowable by the carbon-fiber material (approximately 2400 MPa), even considering a safety factor of 0.5. The contact pressure distributions at the maximum speed is shown in Fig. 6, which reveals that $p_i^{(m)}$ is about 15 MPa, thus guaranteeing appropriate adhesion between PMs and rotor yoke at any speed. Furthermore, Fig. 6 highlights that the contact pressures between the different rims are greater than zero, meaning that torque transmission and PM retention are both ensured properly.

B. Electromagnetic FEA

The electromagnetic FEA results are reported from Fig. 7 to Fig. 9. In particular, the magnetic flux density distribution at rated speed (Fig. 7) reveals quite small values compared to magnetic saturation thresholds of the iron core material (approximately 1.3 T), thus magnetic saturation is prevented at any operating condition; this is expected due to the large equivalent airgap of the proposed IRLA-SPM, which results in a weak magnetic exploitation of the iron core material. However, this is an important advantage in terms of minimizing core losses and back-emf magnitudes, enabling high-speed operation. The phase back-emf evolutions achieved at rated speed (Fig. 8) highlight good sinusoidal shapes, quite similar to the ideal ones, and their magnitudes fairly match those obtained by the analytical procedure (Table III). Furthermore, Fig. 9 highlights the electromagnetic torque evolution at rated speed achieved by 2D FEA (blue line) and 3D FEA (red line). The 2D and 3D simulations, which are

TABLE III IRLA-SPM FINAL GEOMETRY

Description	Symbol	Unit	Value
Rated power	P_n	kW	8
Storable/deliverable energy	E	kWh	8
Rated speed	$\omega_{m,n}$	krpm	6
Maximum speed	$\omega_{m,max}$	krpm	18
Rated torque	T_e	Nm	12.7
Rated current	I_n	A	61
Rated voltage	E_n	V	87
Pole pairs number	p	-	1
Magnetic ratio	α	-	0.68
Turns per phase	n_{turn}	-	28
Winding cross section (single turn)	s_w	mm^2	10
Current density	A_c	A/mm^2	10
Radial interferences	δ_1, δ_j	mm	0.2÷0.9
Rotor yoke outer radius	r_{yr}	mm	110
PM thickness	s_m	mm	17
Flywheel/Sleeve thickness	s_s	mm	337
Rim thickness	s_{rim}	mm	48.14
Rim number	n_{rim}	-	7
Stator outer radius	r_{ys}	mm	507
Stator yoke thickness	s_{ys}	mm	24
Slot height	h_s	mm	15
Active length	l_i	mm	164
Slot number	n_{slot}	-	18

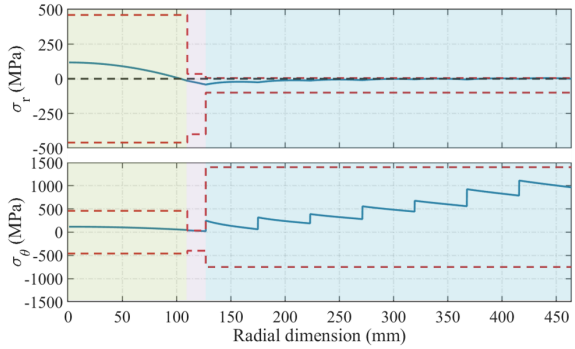

Fig. 4. Radial (top) and tangential (bottom) stress evolutions in the rotor along the radial direction at maximum speed, together with their corresponding boundaries (red-dot lines, which accounts for the safety factor): shaft + rotor yoke (green zone), PMs (purple zone), and flywheel/sleeve (blue zone).

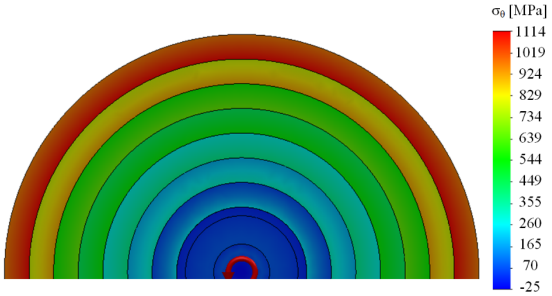

Fig. 5. Tangential stress distributions in the rotor layers at maximum speed.

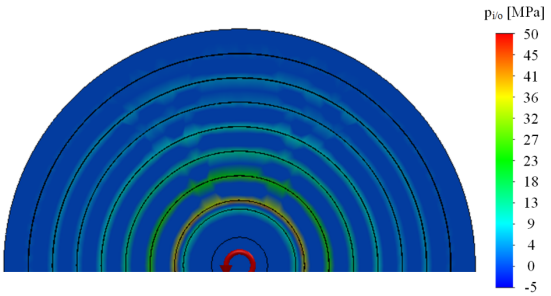

Fig. 6. Contact pressure distribution in the rotor layers at maximum speed.

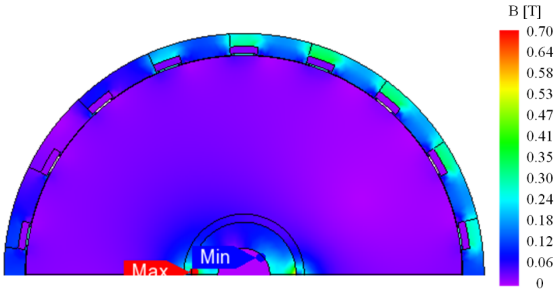

Fig. 7. Magnetic flux density at ω_m = 6 krpm and T_e = 13 Nm.

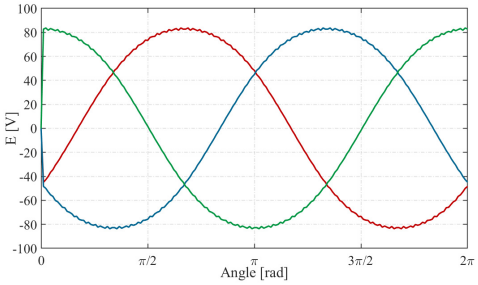

Fig. 8. Back-emf evolutions at rated speed (6 krpm).

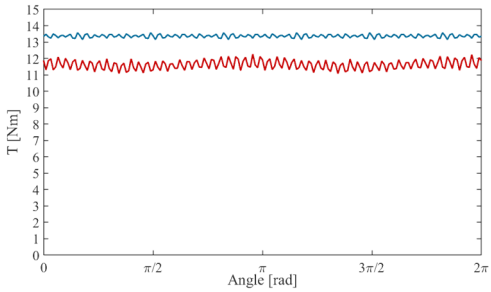

Fig. 9. Torque evolution at rated current (61 A) and speed (6 krpm): 2D FEA (blue line), 3D FEA (red line).

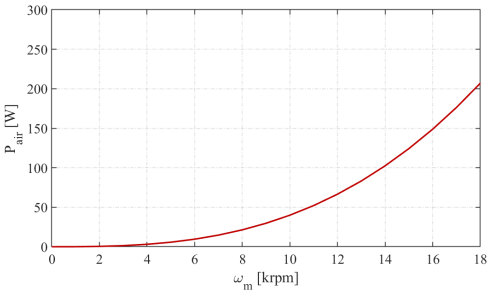

Fig. 10. Friction losses evolution with the rotor speed.

both carried out under the Maximum-Torque-Per-Ampere (MTPA) control strategy, show a rated torque value of 13.3 Nm and 11.6 Nm respectively, with a corresponding torque ripple of approximately 3% and 9%. The worse results achieved by 3D FEA are justified by the presence of a relatively high magnetic flux leakage along the axial direction, which can be evaluated by 3D simulations only and which reduces the IRLA-SPM torque density unsuitably.

C. Losses and efficiency FEA

In order to assess the performances of the proposed IRLA-SPM, overall losses and efficiency analysis has been carried out by using the JMAG software. Different losses contributions have been considered, namely the Joule losses in the windings, the core losses into the iron parts and the mechanical losses due to air friction in the machine airgap (P_{air}) and in the bearings (P_{bear}). Regarding mechanical losses, P_{air} is estimated as in [15]:

$$P_{air} = 0.004\rho_a^{0.8}\beta_a^{0.2}\left(\omega_m r_r\right)^{2.8}\left(2r_r\right)^{1.8}\left(\frac{l_i}{2r_r}+0.33\right) \quad (16)$$

where ρ_a and β_a are the mass density and dynamic viscosity of the fluid in the airgap, while r_r is the rotor outer radius. From (16), it is clear that P_{air} can be reduced acting on the features of the fluid in the airgap. For this reason, a vacuum containment for the IRLA-SPM has been assumed in order to reduce the air density and dynamic viscosity appropriately, so that the air drag and the related mechanical losses can be reduced as well. The evolution of P_{air} with ω_m is shown in Fig. 10, which has been obtained by assuming a pressure inside the containment of about $5\cdot10^{-4}$ bar in accordance with the typical features of the vacuum pumps on the market; this results in a value of ρ_a and β_a of approximately $6\cdot10^{-5}$ kg/m^3 and $1.5\cdot10^{-5}$ Pa·s, respectively. Consequently, Fig. 10 shows that P_{air} exhibits the maximum value (approximately 207 W) at maximum speed (18 krpm), while it decreases quickly as the rotor speed approaches its rated value (6 krpm). On the other hand, P_{bear} is evaluated as in [16]:

$$P_{bear} = n_{bear}\,0.5\cdot\omega_m\mu F D_{bear} \quad (17)$$

in which n_{bear} is the number of bearings used (equal to 2 in this case), μ is the friction coefficient (assumed equal to 0.0010), F is the bearing load and D_{bear} is the inner diameter of the bearing, which is assumed equal to 45 mm.

The losses and efficiency maps of the proposed IRLA-SPM are reported in Fig. 11 and Fig. 12, which are obtained considering the MTPA-Flux-Weakening (MTPA-FW) control strategy directly implemented by the JMAG software package itself. In order to guarantee the required IRLA-SPM dynamic performance at any speed, the DC-link voltage has been set to 320 V in accordance with typical values occurring for single-phase power system connection. Consequently, Fig. 11 shows the overall losses of IRLA-SPM, which increase with both torque and speed. In particular, when the torque increases, the machine suffers from increased Joule losses due to increased phase currents. On the other hand, the

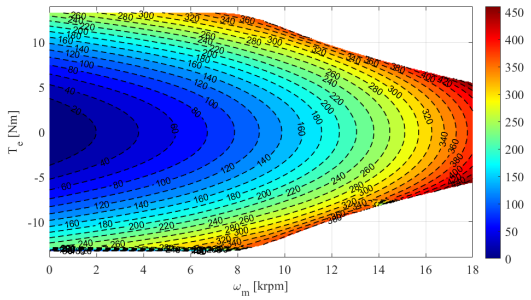

Fig. 11. Losses map of IRLA-SPM (in W).

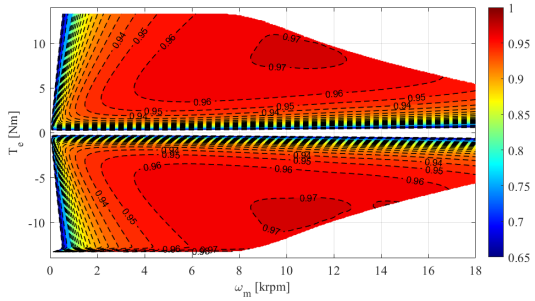

Fig. 12. Efficiency map of IRLA-SPM.

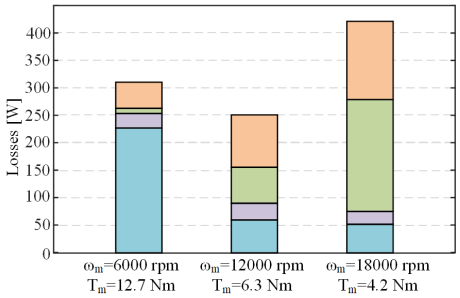

Fig. 13. Losses distribution at different operating conditions: copper (blue), core (purple), rotor friction (green) and bearing losses (orange).

losses increase with rotor speed mainly due to P_{air} and P_{bear}, thus justifying the curled shape of the level curves shown in Fig. 11. The efficiency map shown in Fig. 12 reveals that the proposed IRLA-SPM performs well on almost the overall operating range, but especially in the range between rated and maximum speed, with a maximum efficiency value of approximately 97%.

Considering now three specific operating conditions, all characterized by the rated power (8 kW) but by different speeds (6, 12 and 18 krpm), the corresponding results are shown in Fig. 13 and Table I. When relatively high torque is concerned (at 6 krpm), copper losses are the most significant contribution. Differently, when the speed increases, mechanical losses (P_{air}+P_{bear}) becomes predominant, while core losses present relatively low values at all operating conditions due to the very low magnetic flux density, as foreseen. Among these three cases, the best operating condition in terms of efficiency is achieved at 12 krpm, whereas lower and higher speed values lead to increased losses due to additional Joule or friction losses. It is worth noting that Table I also highlights the losses that occur at the same speed values but in stand-by operating mode. In this regard, the stand-by torque that compensates for mechanical resistance due to air friction and bearing losses at any speed has been evaluated in accordance with (16) as

$$T_{\text{stand-by}} = \frac{\rho_a^{0.8}\beta_a^{0.2}r_r^{4.6}}{7.1787}\left(\frac{l_i}{2r_r}+0.33\right)\omega_m^{1.8}+n_{bear}\,0.5\mu F D_{bear} \quad (18)$$

The results reported in Table I reveal relatively low stand-by losses, which, however, could not guarantee storing energy effectively for long time periods, as foreseen.

D. *Thermal FEA*

The thermal FEA focuses on the distribution of the temperature in each part of the IRLA-SPM, and it has been carried out through the JMAG software. The FEA simulation refer to two of the three operating conditions above-mentioned, namely 8 kW and 6/18 krpm. For both simulations, the losses generated in the different parts of IRLA-SPM have been considered, together with a cooling system set in the external surface of the stator, which guarantees a rapid extraction of the heat generated inside it. Differently, the very low air density in the airgap due to the vacuum containment prevents an effective heat extraction from the rotor, as expected.

Considering Fig. 14 at first, the main heat source is the winding, which is characterized by the highest losses contribution (Fig. 13) and whose maximum temperature is approximately 76 °C. Contrariwise, Fig. 15 shows that the maximum temperature occurs into the rotor due to the higher friction losses achieved at this operating condition. In this case, the maximum temperature is approximately 89 °C. It is worth noting that both these maximum values are significantly below the maximum operating temperature of ferrite PMs (approximately 200°C); this is also due to the low losses caused by ferrite PM, thus justifying the use of this kind of PMs for the proposed IRLA-SPM.

V. Conclusion

The design of an Inner-Rotor Large-Airgap Surface-Mounted Permanent Magnet Synchronous Machine (IRLA-SPM) that integrates a carbon-fiber flywheel has been presented in this paper. The preliminary design has been achieved by a multi-parameter analytical design procedure that refers to appropriate mechanical, electromagnetic, and energy models. The effectiveness of the preliminary design has been then validated by finite element analyses, which have regarded mechanical, electromagnetic, energy, and

TABLE I IRLA-SPM OVERALL LOSSES AT DIFFERENT OPERATING CONDITIONS (8 KW, 6/12/18 KRPM)

Operating condition	Rotor speed [rpm]	Torque [Nm]	Copper Losses [W]	Core Losses [W]	Mechanical Losses [W]	Overall Losses [W]	Efficiency [%]
Rated power	6000	12.7	231.0	26.9	58.0	315.9	96.0
	12000	6.3	61.0	30.9	163.5	255.4	96.8
	18000	4.2	52.9	23.7	352.0	428.6	94.6
Stand-by power	6000	0.053	~ 0	10.6	58.0	20.1	-
	12000	0.090	~ 0	27.5	163.5	94.0	-
	18000	0.145	12.5	24.5	352.0	244.0	-

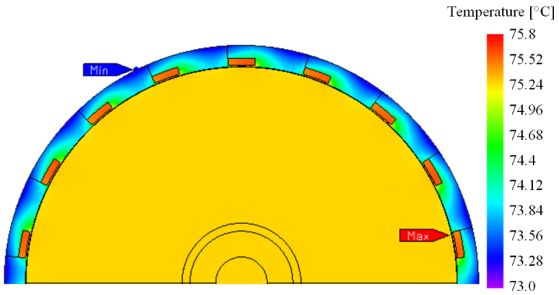

Fig. 14. Temperature distribution at 8 kW and ω_m =6 krpm.

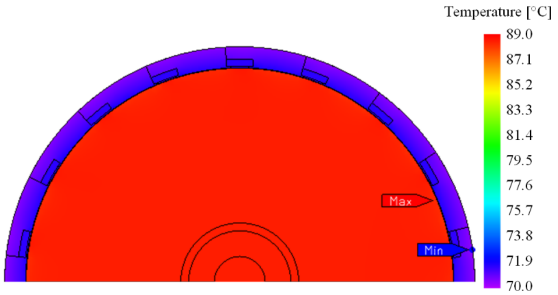

Fig. 15. Temperature distribution at 8 kW and ω_m =18 krpm.

thermal aspects. The results reveal IRLA-SPM a very promising solution for flywheel energy storage systems that should compete with electrochemical batteries in residential applications, especially due to its high efficiency at different operating conditions. However, further investigations and refinements are needed, among which a reduction of stand-by losses and extensive performance assessments by using typical daily load profiles. A prototyping stage is also foreseen for experimental validation. All these aspects will be considered in future works.

VI. References

[1] A. A. K. Arani, H. Karami, G. B. Gharehpetian, and M. S. A. Hejazi, 'Review of Flywheel Energy Storage Systems structures and applications in power systems and microgrids', *Renewable and Sustainable Energy Reviews*, vol. 69, pp. 9–18, Mar. 2017.

[2] R. Sebastián and R. Peña Alzola, 'Flywheel energy storage systems: Review and simulation for an isolated wind power system', *Renewable and Sustainable Energy Reviews*, vol. 16, no. 9, pp. 6803–6813, Dec. 2012.

[3] Z. Jiancheng, H. Lipei, C. Zhiye, and W. Su, 'Research on flywheel energy storage system for power quality', in *Proceedings. International Conference on Power System Technology*, Oct. 2002, vol. 1, pp. 496–499 vol.1.

[4] S. M. Mousavi G, F. Faraji, A. Majazi, and K. Al-Haddad, 'A comprehensive review of Flywheel Energy Storage System technology', *Renewable and Sustainable Energy Reviews*, vol. 67, pp. 477–490, Jan. 2017.

[5] P. Yulong, A. Cavagnino, S. Vaschetto, C. Feng, and A. Tenconi, 'Flywheel energy storage systems for power systems application', in *Proc. of 6th International Conference on Clean Electrical Power (ICCEP 2017)*, Jun. 2017, pp. 492–501.

[6] X. Li, N. Erd, and A. Binder, 'Design and calculation of a 130 kW high-speed permanent magnet synchronous machine in flywheel energy storage systems for urban railway application', in *Proc. of 6th International Conference on Clean Electrical Power (ICCEP 2017)*, Jun. 2017, pp. 452–459.

[7] H. Thomaschewski, T. Turnbull, J. Sandercock, T. Matthews, J. P. Prévost, and S. Deleanu, 'Illustration of flywheel energy storage system performance for engineering technology students', in *Proc. of International Conference on Modern Power Systems (MPS 2017)*, Jun. 2017, pp. 1–8.

[8] G. Fois, A. Floris, A. Serpi, M. Porru, and A. Damiano, 'Design criteria for ferrite-based high-speed permanent magnet synchronous machines', in *Proc. of 7th International Electric Drives Production Conference (EDPC 2017)*, Dec. 2017, pp. 1–7.

[9] A. Damiano, A. Floris, G. Fois, I. Marongiu, M. Porru, and A. Serpi, 'Design of a High-Speed Ferrite-Based Brushless DC Machine for Electric Vehicles', *IEEE Transactions on Industry Applications*, vol. 53, no. 5, pp. 4279–4287, Sep. 2017.

[10] A. Floris, A. Serpi, M. Porru, G. Fois, and A. Damiano, 'Design of a Double-Stage Magnetic Gear for High-Speed Electric Propulsion Systems', in *Proc. of XIII International Conference on Electrical Machines (ICEM'2018)*, Sep. 2018, pp. 670–676.

[11] J. Brunbauer and G. Pinter, 'Effects of mean stress and fibre volume content on the fatigue-induced damage mechanisms in CFRP', *International Journal of Fatigue*, vol. 75, pp. 28–38, Jun. 2015.

[12] S. Ha, H. Han, and Y. Han, 'Design and Manufacture of a Composite Flywheel Press-Fit Multi-Rim Rotor', *Journal of Reinforced Plastics and Composites - J REINF PLAST COMPOSITE*, vol. 27, pp. 953–965, Jan. 2008.

[13] S. J. Kim, K. Hayat, S. U. Nasir, and S. K. Ha, 'Design and fabrication of hybrid composite hubs for a multi-rim flywheel energy storage system', *Composite Structures*, vol. 107, pp. 19–29, Jan. 2014.

[14] L. Chen and C. Zhu, 'Strength Analysis for Surface-mounted Permanent Magnet Rotor in High-Speed Motor', *TELKOMNIKA Indonesian Journal of Electrical Engineering*, vol. 12, no. 10, pp. 7131–7142, Oct. 2014.

[15] D. R. Aitchison, M. Cirrincione, and N. Leijtens, 'Design development of a flywheel energy storage system for isolated Pacific Island communities', in *Proc. of 2016 IEEE International Conference on Advanced Intelligent Mechatronics (AIM)*, Jul. 2016, pp. 1628–1633.

[16] J. Pyrhonen, T. Jokinen, and V. Hrabovcová, *Design of rotating electrical machines*. Chichester, West Sussex, United Kingdom ; Hoboken, NJ: Wiley, 2008.

VII. Biographies

Andrea Floris (S'17) received the bachelor's degree in mechanical engineering, and the master's degree in energy engineering from the University of Cagliari, Italy, in 2012 and 2015, respectively. In 2020 he received the Ph.D degree in electronic and computer engineering at the same university. Dr. Floris is currently doing research at the Department of Electrical and Electronic Engineering of the same university. He is co-author of nine papers published in international conference proceedings and journals. His research activity regards the design of high-speed electrical machines, flywheel energy storage systems and magnetic gear transmission systems for electric vehicles.

Alfonso Damiano (M'11-SM'20) received the master's degree in electrical engineering from the University of Cagliari, Italy, in 1992. In 1994, he joined the Department of Electrical and Electronic Engineering of the same university as an Assistant Professor, where he became Associate Professor (from 2001 to 2018) and, then Full Professor (since 2018) of electrical machines and energy management. He has co-authored more than 170 papers published in international conference proceedings and journals. His current research interests include multiphase and high-speed electrical machines and drives, management and control of electric vehicles, and energy storage systems. Prof. Damiano is a reviewer for several international conferences and journals. He received an IEEE Paper Award.

Alessandro Serpi (M'12) received the master's degree in electrical engineering and the Ph.D. in industrial engineering at the University of Cagliari, Italy, in 2004 and 2009, respectively. From 2009 to 2015 he was a postdoctoral researcher at the Department of Electrical and Electronic Engineering of the same university, where he is now an Assistant Professor (since 2015). Dr. Serpi has been also proposing associate, co-founder, Chief Executive and Technology Officer of NEPSY srl, an academic spin-off company dealing with novel and highly integrated electric propulsion systems. He is co-author of approximately 90 papers published in international conference proceedings and journals. His research activity focuses on management, design and control of electrical machines, drives and energy storage systems. Dr. Serpi is a reviewer for several international conferences and journals. He received two IEEE awards.